DOI: 10.1002/ejic.201000465

Self-Assembly and the Properties of a Highly Oriented Hierarchical Nanobelt–Nanoprism Array of Ternary Oxide Zn–In–O

Nan Pan,[a] Haizhou Xue,[a] Jinhua Huang,[a] Guanghui Zhang,[b] Yukun Wu,[b] Ming Li,[a] Xiaoping Wang,*[a,b] and Jianguo Hou[a]

Keywords: Nanostructures / Doping / Superlattices / Zinc / Indium

A highly oriented, well-aligned hierarchical Zn–In–O nanobelt–nanoprism array was synthesized by vapor-phase transport and condensation using GaN epilayer as the substrate. The upper nanobelts are found to be ZnO:In with an average Zn/In molar ratio of approximately 9:1, and the subjacent nanoprisms are found to be $In_2O_3(ZnO)_m$ (m = 2, 3, 4, and 5) structures. During self-assembly, the nanoprisms are vertically grown on GaN and well aligned along the superlattice stacking direction, upon which each nanobelt is horizontally grown along its [10–10] direction. The spatially resolved cathodoluminescence spectra collected on individual hierarchical nanostructures clearly show characteristics for the ZnO:In nanobelt and for the $In_2O_3(ZnO)_m$ nanoprism, which are distinctly different from the emissions of the undoped ZnO nanorod. *I*-*V* measurements on individual nanobelts reveal good conductivity over 10^3 S m^{-1} and high electron concentration of 10^{19}–10^{20} cm^{-3}. This bottom-up self-assembled, highly oriented, and well-aligned hierarchical nanoarray may find applications in newly emerging vertically integrated nanoarray circuits.

Introduction

The past half-century has witnessed roaring success in the practical application of semiconductor integrated circuits, which have thoroughly changed our daily lives. Behind this huge success was precise doping control and the realization of manmade superlattice structures on two-dimensional (2D) materials (films) that brought such splendid achievements in state-of-the-art semiconductor microelectronic devices. Similarly, the practical device applications of one-dimensional (1D) nanomaterials also depend greatly on the materials' doping and superlattice control. For this reason, the doping as well as the formation of heterostructures and superlattice structures of 1D nanomaterials have been extensively studied for years.[1–9] To synthesize 1D hetero- or superstructured nanomaterials, accurate but costly layer-by-layer growth techniques, such as ultrahigh-vacuum (UHV) molecular-beam epitaxy (MBE) and metallorganic vapor-phase epitaxy [MOVPE, also called as metallorganic chemical-vapor deposition (MOCVD) or chemical-beam epitaxy (CBE)], have to be exploited with rare exceptions.[10–12] By these means, high-quality 1D hetero- and superstructures can be controllably fabricated with atomic-level precision; however, the complexity and the cost of such an approach hindered their mass production and practical application. Besides, the implantation-based doping strategy, which had been a great success for bulk and 2D materials, was found to be either inapplicable or unsatisfactory for 1D nanostructures due to the serious "self-purification" or segregation effect.[13,14] In other words, to the best of our knowledge, the simple but efficient, low-cost, mass-produced preparation of 1D doped, hetero- and superstructures is still a challenge.

Spontaneously formed superlattices and doping in certain 1D nanomaterials (such as in 1D ZnO systems)[15–19] by means of simple self-assembly offers an alternative way to produce such advanced structures, which is cheaper, more time-saving, and much easier to realize, and therefore has the promise for practical applications; however, one of the serious concerns may be the quality of the self-assembly by this approach. In fact, due to the dramatic structural modulations by doping and/or superlattice formation, the assembly qualities of the above-mentioned advanced nanostructures are greatly degraded. Taking In-doped ZnO 1D nanostructures as an example, it has been found that the growth direction and the morphology of the nanostructures can be dramatically changed due to In doping.[20–23] However, nanodevice applications require not only the doping and the superlattice realizations for these 1D nanostructures but also the good order and high quality of the self-assembly (which is crucial for the integration); clearly, the current approaches based on self-assembly cannot meet this criterion and more efforts are therefore urgently needed. Furthermore, few efforts have been made to improve the

[a] Hefei National Laboratory for Physical Sciences at the Microscale, University of Science and Technology of China, Hefei, Anhui 230026, P. R. China
[b] Department of Physics, University of Science and Technology of China, Hefei, Anhui 230026, P. R. China
Fax: +86-551-3606266
E-mail: xpwang@ustc.edu.cn

Supporting information for this article is available on the WWW under http://dx.doi.org/10.1002/ejic.201000465.

quality of hierarchical 1D nanostructure assembly[24,25] despite its importance in building bottom-up, self-assembled 1D nanomaterial circuits.

In this paper, we report the self-assembly of a highly oriented, well-aligned hierarchical nanobelt–nanoprism array of ternary oxide Zn–In–O, through which the $In_2O_3(ZnO)_m$ (m = 2, 3, 4, and 5) nanoprisms are vertically grown on the substrate and well aligned along the superlattice stacking direction; on the top of the nanoprisms each ZnO:In nanobelt is horizontally grown along its [10–10] direction. Although complex in structure and morphology, this hierarchical nanoarray is of exceptionally good alignment and possesses high in-plane symmetry, thus demonstrating the high quality of the self-assembly. The optical properties of the individual hierarchical nanostructures (including the nanobelt and the nanoprism) have been studied by spatially resolved cathodoluminescence (CL), and the electrical properties of the single ZnO:In nanobelts have also been investigated.

Results and Discussion

The typical morphology of the hierarchical nanobelt–nanoprism array is shown in Figure 1, b–d. For a clear comparison, the morphology of the undoped ZnO nanorod array is also shown (Figure 1, a). As seen, both the samples, despite their drastically different morphologies, are well aligned and highly oriented because of the high quality of the growth substrate [GaN (0001) epilayer on c-sapphire; the full-width half-maximum (FWHM) values of the (0004) rocking curve and the (10–11) Φ scan are 0.08 and 0.23°, respectively]. From Figure 1, a and c, one can clearly observe the in-plane symmetry of the two kinds of arrays, which can be further confirmed by the FFT pattern in the inset of Figure 1, c for the nanobelt–nanoprism array. However, unlike the undoped ZnO nanorods grown vertically from the substrate and well aligned along the axial direction, the nanobelt–nanoprism array clearly exhibits a hierarchical morphology in which the vertical growth of the nanoprism along the axis is substituted by the subsequent horizontal growth of the nanobelt, thereby demonstrating a sharp switch in the growth direction during the structure formation. To obtain the morphological information in more detail, the standup hierarchical sample was carefully brought down and transferred onto a clean silicon wafer by means of a polydimethylsiloxane (PDMS) stamp,[26] then characterized by field-emission scanning electron microscopy (FESEM). As shown in Figure 1, d, a typical individual hierarchical structure includes an upper nanobelt and a subjacent nanoprism support. Statistics from the FESEM observation show that the nanobelts are 3–5 μm in length, around 200 nm in width, and no more than 40 nm in thickness; the subjacent laminative nanoprisms are no more than 2 μm in length with the diameters gradually decreased from around 400 to around 150 nm (from the bottom to the top).

To analyze the structure of the samples, an XRD 2θ scan was performed for the GaN substrate, the undoped nanorod array, and the hierarchical nanobelt–nanoprism array. The result is shown in Figure S2 in the Supporting Information. As can be seen, the strong peaks from the ZnO and GaN (0002) diffraction (which overlap each other) as well as the clear peaks from the ZnO and GaN (0004) diffractions (which are separated) can be found for both the undoped (curve 2) and the doped (curve 3) samples, thereby indicating that the main products are both wurtzite ZnO. However, unlike the GaN substrate (curve 1) and the undoped nanorod, the hierarchical sample shows a series of specific diffractions at the low-angle region, which can be further revealed by the low-angle fine scan (curve 4). The low-angle fine scan result of the as-grown hierarchical nanoarray is shown in Figure 2 for more clarity (logarithm intensity is used for the weak peak identification). As shown in Figure 2 and Table S1 (see the Supporting Information), all of the observed peaks can be indexed to certain

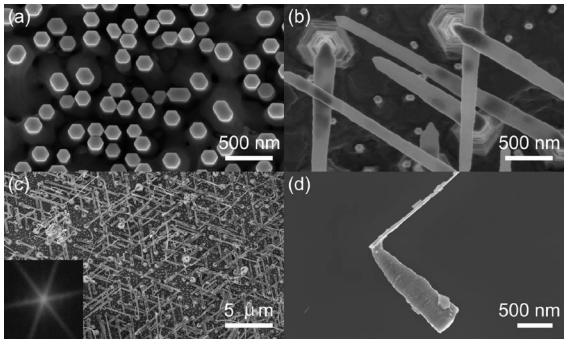

Figure 1. The top-view FESEM images of the highly oriented (a) well-aligned undoped ZnO nanorod array as well as (b, c) the hierarchical nanobelt-nanoprism array of Zn–In–O. (b) and (c) are the higher- and lower-magnification images of the hierarchical nanoarray, respectively. The inset in (c) is the corresponding fast Fourier transform (FFT) pattern. (d) An individual side-lying nanobelt–nanoprism structure transferred onto a clean Si wafer.

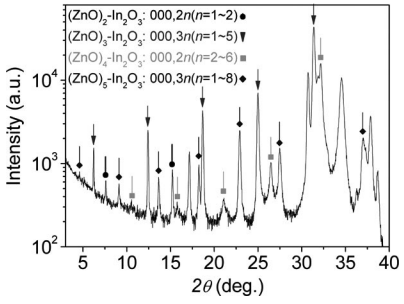

Figure 2. The low-angle XRD 2θ scan result for the hierarchical nanobelt–nanoprism array. The circle (●), triangle (▼), square (■), and diamond (♦) mark a series of diffraction peaks from $In_2O_3(ZnO)_2$, $In_2O_3(ZnO)_3$, $In_2O_3(ZnO)_4$, and $In_2O_3(ZnO)_5$, respectively. From the small to the large 2θ region (from left to right), the circles denote the (0002) and (0004) diffractions of $In_2O_3(ZnO)_2$; the triangles denote the (0003), (0006), (0009), (000,12), and (000,15) peaks of $In_2O_3(ZnO)_3$; the squares denote the (0004), (0006), (0008), (000,10), and (000,12) peaks of $In_2O_3(ZnO)_4$; whereas the diamonds denote the (0003), (0006), (0009), (000,12), (000,15), (000,18), and (000,24) peaks of $In_2O_3(ZnO)_5$. The peaks not marked here can also be indexed to certain diffractions of the above four structures (Table S1 in the Supporting Information).

diffractions from the homologous compounds with a chemical formula of $In_2O_3(ZnO)_m$ (m = integer); further analysis reveals that $In_2O_3(ZnO)_m$ with m = 2, 3, 4, and 5 all existed in the hierarchical nanobelt–nanoprism array. In the studies on ZnO nanostructures, dominant ZnO (0002) and (0004) diffractions are regarded as a feature of good alignment and uniform orientation along the c axis. Similarly, for the hierarchical nanostructures, the dominant diffractions from the (000, l) planes (l are a series of integers identified in Figure 2) of $In_2O_3(ZnO)_m$ (m = 2, 3, 4, and 5) are also a characteristic, thus indicating good alignment along the superlattice stacking direction. This result is highly consistent with the FESEM observations.

Although we have found that $In_2O_3(ZnO)_m$ (m = 2, 3, 4, and 5) exist in the hierarchical nanoarray in considerable quantity, the microstructure and the composition of an individual nanobelt–nanoprism are still unclear. To this end, the sample was transferred and characterized in an analytic electron microscope for high-resolution transmission electron microscopy (HRTEM) and energy-dispersive spectroscopy (EDS). The results of the nanobelts in the hierarchical nanostructures are shown in Figure 3 and Figure S3 in the Supporting Information. As can be seen, the nanobelts are In-doped ZnO with an average Zn/In molar ratio of approximately 9:1 (Figure S3); they grow along their [10–10] direction and possess extremely larger polar surfaces of (000 ± 1). HRTEM and selected-area electron diffraction (SAED) recorded from the side-lying nanobelt further reveal the existence of the stacking faults along the c axis. The switched growth direction from [0001] to [10–10], the existence of large polar surfaces, and the stacking faults are in good agreement with the previous reports[21,27] on In-doped ZnO nanobelts; therefore, the switch in direction here and the stacking fault formation during the growth

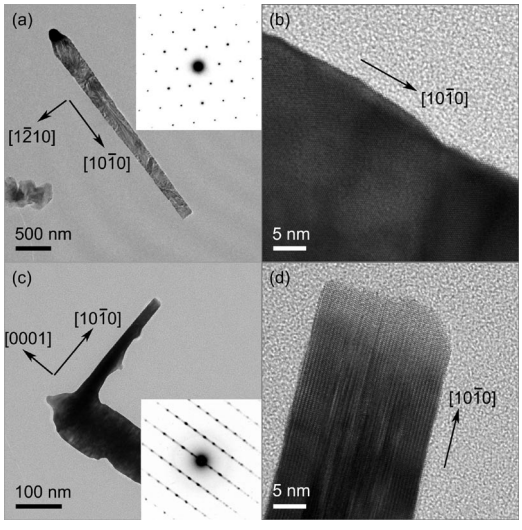

Figure 3. The HRTEM characterizations of the nanobelts in the hierarchical nanostructures. (a) The morphology and (b) the HRTEM image of a prone nanobelt. The inset in (a) is the corresponding SAED pattern. (c) The morphology and (d) the HRTEM image of a side-lying nanobelt. The inset in (c) is the corresponding SAED pattern.

should also be attributed to the structural modulation induced by In doping. It is worth mentioning that in most previous studies, successful doping will usually be accompanied by the degradation of the alignment/symmetry for a nanostructure array; in contrast, here, not only is successful In doping achieved for the ZnO nanobelts but also the alignment and in-plane symmetry is well preserved. Unlike the nanobelt, the subjacent nanoprism in the hierarchical nanostructure is too thick to obtain HRTEM and satisfactory SAED (the diameter is as large as several hundred nanometers and is changed from one end to the other); however, since $In_2O_3(ZnO)_m$ (m = 2, 3, 4, and 5) exist in considerable quantity and are absent in the ZnO:In nanobelts, they must exist in the subjacent laminative nanoprisms. Although the direct observation of the $In_2O_3(ZnO)_m$ superstructures from HRTEM is difficult, EDS can be conducted to identify the elementary composition. The nominal stoichiometric proportion of Zn/In should respectively be 1:1, 1.5:1, 2:1, and 2.5:1 for $In_2O_3(ZnO)_m$ when m = 2, 3, 4, and 5. In this study, EDS recorded on two typical nanoprisms give different Zn/In molar ratios of 1.95:1 and 2.57:1 (Figure S4 in the Supporting Information), which perfectly agree with the stoichiometry of $In_2O_3(ZnO)_4$ and $In_2O_3(ZnO)_5$. This result is an alternative but solid evidence that the $In_2O_3(ZnO)_m$ structures do exist in the nanoprisms instead of the upper nanobelts.

From the above analysis, we can conclude that the hierarchical nanostructures contain two components: the upper ZnO:In nanobelt with a Zn/In molar ratio of approximately 9:1, and the subjacent $In_2O_3(ZnO)_m$ (m = 2, 3, 4, and 5) nanoprisms. The nanoprisms are vertically grown (on GaN) and well aligned along the superlattice stacking direction, whereas each nanobelt is horizontally grown along its [10–10] direction from the top of a nanoprism. For both the nanoprisms and the nanobelts, the in-plane symmetry of the high-quality GaN epilayer is inherited, thus indicating the epitaxial nature of the hierarchical nanostructure growth.

Besides the switch in the growth direction, it may also seem strange that there is a distinctly nonhomogeneous In distribution in the hierarchical nanostructure, in which the In/Zn ratio is respectively much higher in the nanoprism (≥1:2.5) and dramatically lower in the nanobelt (ca. 1:9) than that in the precursor (1:3.5). Further inspection on the formation process of these hierarchical structures is therefore needed. To look into the growth mechanism, a series of control experiments have been performed in which various sample temperatures (Figure S5 in the Supporting Information) and different oxygen concentrations (Figure S6 in the Supporting Information) were applied. Based on these results, we suggest that the ZnO:In polar nanobelts are formed during the cooling process. At the initial stage of cooling (at which the sample temperature is reduced from around 700 to 400–500 °C), the temperature is still fairly favorable for polar nanobelt growth;[28] with sufficiently high O/Zn ratios, it can longitudinally grow up efficiently.[29] However, as the In vapor pressure drastically decreases with the reduced temperature within this range

(whereas that of Zn does not change that much),[30] this drop will certainly affect the In content in the nanobelts. As a result, the In/Zn ratio in the nanobelt is found to be much lower than either the precursor or the nanoprism. Since the change of In vapor pressure is much more violent than that of Zn within the range from 800–500 °C, the Zn/In ratio in the products can therefore be widely tuned by varying the local temperature/In vapor concentration of the sample.

At present it is still not clear what the exact driving force is that switches the growth from the vertical to the horizontal; however, the superlattice probably accounts for this switch, since the superlattice (compared with the formation of In_2O_3 segregation) is energetically metastable and inevitably contains lattice strain and interfacial polarization, the nanoprism has to find a way to effectively relax its excess energy. To taper itself is one way; to switch the growth direction is another efficient one.[22] Apparently, the growth of such a hierarchical system is quite complex. To ultimately unravel the exact growth mechanism, more experiments and theoretical methods (such as molecular dynamics) have to be involved. More efforts on these are to be carried out urgently in the future.

Besides the distinct microstructures and stoichiometric proportions, the physical properties of ZnO:In and $In_2O_3(ZnO)_m$ such as luminescence are also expected to be drastically different. The (optical) band gap of the superlattice structures can differ remarkably from that of a ZnO material.[18] To study the luminescence of the ZnO:In nanobelt and the $In_2O_3(ZnO)_m$ nanoprism, the transferred individual hierarchical nanostructures were probed by spatially resolved cathodoluminescence (CL) and the results are shown in Figure 4. For comparison, the representative CL spectrum of an undoped ZnO nanorod is also collected. As shown in Figure 4, d, the CL spectra of the ZnO:In nanobelt and the $In_2O_3(ZnO)_m$ nanoprism are distinctly different from that of the undoped ZnO nanorod. For the undoped nanorod, a dominant emission at 382 nm (3.246 eV) can be found and assigned to the near band edge (NBE) emission of excitons in ZnO.[31] Besides the NBE emission, a weak but broad emission centered at around 510 nm (2.431 eV) is also observable, which can be attributed to the recombination from deep levels (DL).[32] In previous work, we have demonstrated that this DL emission is dominantly surface related.[33] In contrast, the ZnO:In nanobelt has a dominant emission peak in the visible region, the asymmetric nature of this peak indicates that the recombination contain multiple pathways and their origins are probably different. Compared to the undoped nanorod, the In-doped nanobelt also has an NBE peak in the ultraviolet region; however, the peak position is redshifted to 388 nm (3.196 eV; the corresponding energy redshift is as large as ≈50 meV), and the FWHM of the peak is also broadened from around 26 nm to around 40 nm. Such a redshift and a broadening of the NBE emission can be respectively attributed to the band gap narrowing effect[27,34] induced by heavy doping of In and the band tailing due to the formation of impurities or defects,[27] which also indicates the heavy doping nature of the ZnO:In nanobelt. Unlike the undoped and doped ZnO nanostructures, the CL spectra from individual $In_2O_3(ZnO)_m$ nanoprisms show no NBE emission in the ultraviolet region. A symmetric and broad emission centered at around 536 nm (2.313 eV) is exclusively observable, which is in good agreement with the previous reports on $In_2O_3(ZnO)_m$ nanostructures[15,16,18] and can be assigned to the recombination from the In-related centers. Since the visible emission of the nanobelt is quite complex and apparently contains more than one peak, we performed multipeak fitting for it.

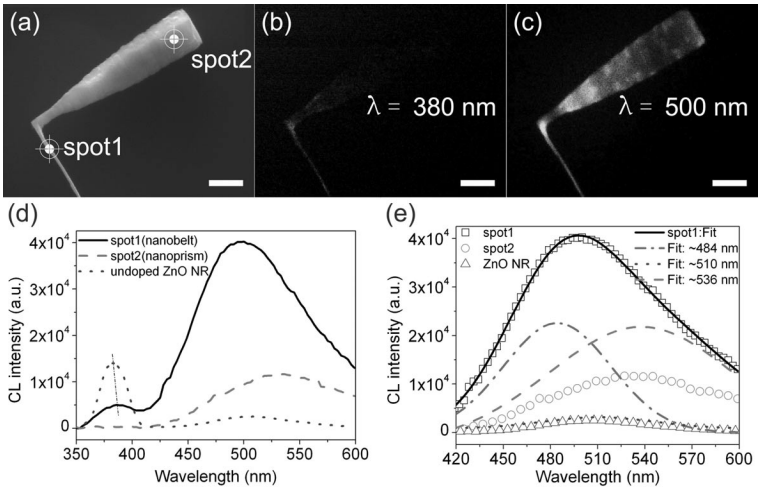

Figure 4. The spatially resolved CL spectra of the ZnO:In nanobelt and $In_2O_3(ZnO)_m$ nanoprism. (a) The morphology of an individual hierarchical nanostructure. The marked points, namely, spot1 and spot2, denote the positions of the electron-beam excitation. (b) The corresponding monochromatic CL images collected at the emission wavelengths of 380 nm and (c) 500 nm. The scale bars in (a–c) are 500 nm. (d) The spatially resolved CL spectra of a ZnO:In nanobelt (the solid line), an $In_2O_3(ZnO)_m$ nanoprism (the dashed line), and an undoped ZnO nanorod (the dotted line). (e) The emissions in the visible region for (c) and the multipeak fitting result of the nanobelt visible emission. The fitting curve with the peak at around 510 nm (dotted line) is overlapped with the experimental spectrum of the undoped ZnO nanorod (hollow triangle). All the CL images and spectra are recorded at room temperature.

It was very interesting to find that the asymmetric peak can be satisfactorily fitted by three Gaussian peaks centered at approximately 484, 510, and 538 nm, respectively (namely, 2.562, 2.431, and 2.305 eV). The peaks at around 510 nm (the dotted line in Figure 4, e) and around 538 nm (the dashed line in Figure 4, e) are in good accord with the surface-related DL emission of the undoped ZnO nanorod (the triangles in part e of Figure 4, which are almost overlapped with the dotted line) and the In-related recombination of the $In_2O_3(ZnO)_m$ nanoprism (the circles in Figure 4, e), therefore can be similarly assigned to the DL and the In-related recombination, respectively. The peak at around 484 nm appears to a featured recombination pathway of the nanobelt, of which we do not know the exact origin; one possible mechanism is the recombination from the considerable stacking-fault-type defects in the ZnO:In nanobelt. More efforts are to be made in the future to intensively study the mechanisms and origins of this complex emission.

To further study the doping effect in the ZnO:In nanobelt, prototype single-nanobelt field-effect transistor (FET) devices with a back-gate configuration were fabricated and the *I*–*V* characteristics of the single nanobelts were measured. The upper inset of Figure 5 shows the FESEM image of a 200 nm-wide and 1.33 μm-long nanobelt (only the interelectrode section is considered) contacted by the source and drain electrodes. The typical drain current (I_{sd}) versus bias voltage (V_{sd}) plots of this ZnO:In nanobelt under different gate voltages (V_g = –10, –5, 0, 5, and 10 V) are shown in Figure 5. As can be seen, all the I_{sd}–V_{sd} curves exhibit Ohmic-like behaviors instead of nonlinear and rectifying characteristics. When the V_g changes from –10 to +10 V, the I_{sd}–V_{sd} curves almost overlap each other, thus demonstrating that the gate voltage modulation to the carrier transport in the nanobelt is very small. The gate effect of the single-nanobelt FET is shown in the lower inset of Figure 5, from which we can also see that the I_{sd} hardly changes with the V_g at a constant bias voltage of 0.5 V. Since the transconductance is derivable, the electron mobility (μ_e) of the single-nanobelt FET can be estimated to be approximately 5.5 $cm^2 V^{-1} s^{-1}$, which is drastically lower than the μ_e in ZnO bulk (ca. 180 $cm^2 V^{-1} s^{-1}$)[35] and is also lower than those of the reported single ZnO nanowire, nanorod, or nanobelt FETs[36–39] (in which the μ_e are in the range of 10–100 $cm^2 V^{-1} s^{-1}$ and is seldom below 10 $cm^2 V^{-1} s^{-1}$[40]). The reduced μ_e can be understood through the consideration that the electron scattering is significantly enhanced by the In dopant atoms and the stacking faults in the doped nanobelt. Given the μ_e and the conductivity (σ, which can be calculated from the I_{sd}–V_{sd} curve and the geometrical parameters of the nanobelt), the electron concentration (n_e) of the ZnO:In nanobelt can also be estimated to be approximately 3.8×10^{19} cm^{-3} from the relationship of $\sigma = n_e e \mu_e$. This result unambiguously proves the heavy doping of electrons in the doped nanobelt. It should be pointed out that the estimated electron mobility and concentration for different single ZnO:In nanobelts are fairly consistent, with the μ_e within 1–10 $cm^2 V^{-1} s^{-1}$ and the n_e within 10^{19}–10^{20} cm^{-3}. Such high electron concentrations make the nanobelts "metallic" and therefore the weak gate dependence as well as the Ohmic-like contact behavior is obtained. Benefitting from the good conductivity ($\geq 10^3$ $S m^{-1}$), the high electron concentration, and the horizontal and oriented growth direction (the nanobelts are often found to bridge to others as shown in Figure 1, b), this "metallic" ZnO:In nanobelt may serve as new interconnecting wires in integrated circuits (ICs). The nanobelt is fairly conducting, transparent, and flexible, which can be smartly and exactly "spot-welded" onto the top of each nanoprism by means of simple self-assembly (thus avoiding the complexity in the addressable fabrication of interconnecting wires). This is therefore exceptionally suitable for the interconnection of the vertically integrated 1D nanomaterial circuits[41–43] as well as for applications in which transparency and flexibility features are needed.

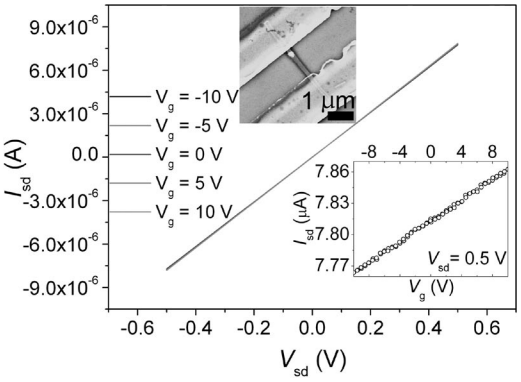

Figure 5. The curves *I*–*V* of a single ZnO:In nanobelt in the hierarchical nanostructure under different gate voltages. Upper inset: the FESEM image of an individual nanobelt between source and drain electrodes. Lower inset: the drain current (I_{sd}) response versus the gate voltage (V_g) at a constant bias voltage (V_{sd}) of 0.5 V.

Conclusion

A kind of highly oriented, well-aligned hierarchical Zn–In–O nanobelt–nanoprism array was successfully grown by vapor-phase transport and condensation by using a GaN epilayer as the substrate. Each hierarchical nanostructure contains two components, the upper ZnO:In nanobelt with an average Zn/In molar ratio of approximately 9:1 and the subjacent $In_2O_3(ZnO)_m$ (m = 2, 3, 4, and 5) nanoprisms. The nanoprisms are vertically grown on GaN and well aligned along the superlattice stacking direction, upon which each nanobelt is horizontally grown along its [10–10] direction. The ZnO:In nanobelt possesses a dominant asymmetric visible emission around 500 nm and a weak, redshifted, and broadened NBE emission at 388 nm, whereas the $In_2O_3(ZnO)_m$ nanoprism exclusively holds a broad visible emission centered at around 536 nm. Both are distinctly different from the emissions of an undoped ZnO nanorod. The emission at around 536 nm is believed to be the recombination from the In-related centers, whereas the redshift and broadening in the NBE emission of the nanobelt are due to the band-gap narrowing and band tailing

induced by doping. Electrical measurements on individual nanobelts reveal good conductivity over 10^3 S m^{-1} and high electron concentration of 10^{19}–10^{20} cm^{-3}. This bottom-up self-assembled, highly oriented, well-aligned hierarchical nanobelt–nanoprism array may be useful in the newly emerging vertical nanoarray integrated circuits. In particular, the good conductivity, the high electron concentration, and the highly oriented horizontal growth features of the ZnO:In nanobelt make it exceptionally suitable for use as the interconnecting component in the vertical nanoarray circuits.

Experimental Section

The highly oriented hierarchical Zn–In–O nanobelt–nanoprism array was prepared by vapor-phase transport and condensation (VPTC)[4] by means of co-evaporating the Zn and In sources at an elevated temperature of about 1000 °C. The preparation details are as follows. A high-quality GaN (0001) layer epitaxially grown on *c*-sapphire, with the FWHM of the GaN (0004) rocking curve as small as 0.08°, was used as the growth substrate. Fine powders of ZnO (99.99%), metallic In (99.99%), and graphite (spectrograde) were weighed and mixed well (by a mortar and pestle) at a molar ratio of 1:2/7:1; these served as the precursors. For each growth, the mixed powders (2 g) were loaded into the closed end of a long and slim quartz tube (16 cm in length and 1 cm in diameter, with only one end open); then the cleaned substrate was carefully pushed into the same quartz tube and separated from the precursors at a horizontal distance of about 8 cm. After this, the quartz tube was inserted into the horizontal alumina tube chamber of a conventional tube furnace. The position of the precursors (the closed end of the quartz tube) was kept at the heating center of the furnace, and the open end of the quartz tube was faced to the upstream of the gas flow. During a typical growth, the alumina tube chamber and pipes were first sealed and evacuated to approximately 0.1 Torr, then the pipes and chamber were rinsed with a high purity argon flow of 200 sccm (sccm = standard cubic centimeter per minute) for about 15 min before the flow was cut off and they were evacuated again. The rinse and evacuation process was repeated for 3 cycles. After that, a constant high-purity argon flow of 50 sccm was set as the carrier gas (which was maintained during the whole heating and cooling process), and the precursors were heated up to 950–1000 °C over 20 min. Once the preset temperature was reached, a high-purity dry-oxygen flow of 50 sccm was introduced, at which the system was maintained for about 1 h before the oxygen flow was cut off and the furnace was simultaneously powered off. Finally, the chamber was naturally cooled down to room temperature and the sample was taken out for characterizations. The highly oriented, well-aligned, undoped ZnO nanorod array was prepared through the same approach as the control sample, all the growth conditions are kept the same except that no In source was added to the ZnO–graphite mixed precursors.

The morphology of the sample was examined by field-emission scanning electron microscopy (FESEM), the structure of the sample was characterized by X-ray diffraction (XRD) and high-resolution transmission electron microscopy (HRTEM), and the composition was analyzed by energy-dispersive spectroscopy (EDS) attached to the HRTEM. The luminescence property of the individual nanostructure was investigated by spatially resolved cathodoluminescence (CL; the experiment was conducted with a FESEM equipped with a Gatan MonoCL3 system). The single-nanobelt field-effect transistor (FET) devices were fabricated by a standard microprocessing technique with a gate dielectric (Si_3N_4) thickness of 300 nm. The electrical properties of the devices were recorded with a Keithley 4200 instrument. Both the optical and electrical properties were measured at room temperature.

Supporting Information (see also the footnote on the first page of this article): Low-magnification FESEM image of the hierarchical nanoarray; XRD images of the GaN substrate, the undoped ZnO nanorod array, and the hierarchical nanoarray; identification of the low-angle diffraction data; EDS of individual nanobelts and nanoprisms; and control experiments on nanostructure growth in which various sample temperatures and different oxygen concentrations are respectively applied.

Acknowledgments

This work is supported by the National Natural Science Foundation of China (NSFC) (grant nos. 50721091, 10874165, and 90921013), the Ministry of Science and Technology of China (MOST) (grant no. 2006CB922002), and the Chinese Academy of Sciences (CAS). N. P. also thanks the support by the China Postdoctoral Science Foundation (grant no. 20090460737) and the Fundamental Research Funds for the Central Universities (FRFCU).

[1] L. J. Lauhon, M. S. Gudiksen, D. L. Wang, C. M. Lieber, *Nature* **2002**, *420*, 57–61.
[2] Y. Y. Wu, R. Fan, P. D. Yang, *Nano Lett.* **2002**, *2*, 83–86.
[3] M. T. Björk, B. J. Ohlsson, T. Sass, A. I. Persson, C. Thelander, M. H. Magnusson, K. Deppert, L. R. Wallenberg, L. Samuelson, *Nano Lett.* **2002**, *2*, 87–89.
[4] P. D. Yang, *MRS Bull.* **2005**, *30*, 85–91.
[5] J. Xiang, W. Lu, Y. J. Hu, Y. Wu, H. Yan, C. M. Lieber, *Nature* **2006**, *441*, 489–493.
[6] C. Thelander, P. Agarwal, S. Brongersma, J. Eymery, L. F. Feiner, A. Forchel, M. Scheffler, W. Riess, B. J. Ohlsson, U. Gösele, L. Samuelson, *Mater. Today* **2006**, *9*, 28–35.
[7] J. G. Lu, P. C. Chang, Z. Y. Fan, *Mater. Sci. Eng. R-Rep.* **2006**, *52*, 49–91.
[8] B. Z. Tian, T. J. Kempa, C. M. Lieber, *Chem. Soc. Rev.* **2009**, *38*, 16–24.
[9] R. X. Yan, D. Gargas, P. D. Yang, *Nat. Photonics* **2009**, *3*, 569–576.
[10] S. R. Nicewarner-Peña, R. Griffith Freeman, B. D. Reiss, L. He, D. J. Peña, I. D. Walton, R. Cromer, C. D. Keating, M. J. Natan, *Science* **2001**, *294*, 137–141.
[11] S. Han, C. Li, Z. Q. Liu, B. Lei, D. H. Zhang, W. Jin, X. L. Liu, T. Tang, C. W. Zhou, *Nano Lett.* **2004**, *4*, 1241–1246.
[12] Y. Yang, D. S. Kim, M. Knez, R. Scholz, A. Berger, E. Pippel, D. Hesse, U. Gösele, M. Zacharias, *J. Phys. Chem. C* **2008**, *112*, 4068–4074.
[13] M. V. Fernández-Serra, Ch. Adessi, X. Blase, *Phys. Rev. Lett.* **2006**, *96*, 166805.
[14] G. M. Dalpian, J. R. Chelikowsky, *Phys. Rev. Lett.* **2006**, *96*, 226802.
[15] J. S. Jie, G. Z. Wang, X. H. Han, J. G. Hou, *J. Phys. Chem. B* **2004**, *108*, 17027–17031.
[16] C. W. Na, S. Y. Bae, J. H. Park, *J. Phys. Chem. B* **2005**, *109*, 12785–12790.
[17] P. X. Gao, Y. Ding, W. J. Mai, W. L. Hughes, C. S. Lao, Z. L. Wang, *Science* **2005**, *309*, 1700–1704.
[18] B. Alemán, P. Fernández, J. Piqueras, *Appl. Phys. Lett.* **2009**, *95*, 013111.
[19] D. P. Li, G. Z. Wang, X. H. Han, J. S. Jie, S. T. Lee, *J. Phys. Chem. C* **2009**, *113*, 5417–5421.
[20] J. Y. Lao, J. G. Wen, Z. F. Ren, *Nano Lett.* **2002**, *2*, 1287–1291.
[21] Y. Ding, X. Y. Kong, Z. L. Wang, *Phys. Rev. B* **2004**, *70*, 235408.

[22] C. X. Xu, X. W. Sun, Z. L. Dong, G. P. Zhu, Y. P. Cui, *Appl. Phys. Lett.* **2006**, *88*, 093101.
[23] H. J. Fan, B. Fuhrmann, R. Scholz, C. Himcinschi, A. Berger, H. Leipner, A. Dadgar, A. Krost, S. Christiansen, U. Gösele, M. Zacharias, *Nanotechnology* **2006**, *17*, S231.
[24] T. R. Zhang, W. J. Dong, M. Keeter-Brewer, K. Sanjit, R. N. Njabon, Z. R. Tian, *J. Am. Chem. Soc.* **2006**, *128*, 10960–10968.
[25] J.-S. Na, B. Gong, G. Scarel, G. N. Parsons, *ACS Nano* **2009**, *3*, 3191–3199.
[26] E. Delamarche, C. Donzel, F. S. Kamounah, H. Wolf, M. Geissler, R. Stutz, P. Schmidt-Winkel, B. Michel, H. J. Mathieu, K. Schaumburg, *Langmuir* **2003**, *19*, 8749–8758.
[27] J. S. Jie, G. Z. Wang, X. H. Han, Q. X. Yu, Y. Liao, G. P. Li, J. G. Hou, *Chem. Phys. Lett.* **2004**, *387*, 466–470.
[28] X. Y. Kong, Z. L. Wang, *Nano Lett.* **2003**, *3*, 1625–1631.
[29] J. Y. Park, D. J. Lee, S. S. Kim, *Nanotechnology* **2005**, *16*, 2044–2047.
[30] C. B. Alcock in *CRC Handbook of Chemistry and Physics, Internet Version 2007 87th edition* (Ed.: D. R. Lide), Taylor and Francis, Boca Raton, FL, **2007**, section 4, pp. 128–129.
[31] B. K. Meyer, H. Alves, D. M. Hofmann, W. Kriegseis, D. Forster, F. Bertram, J. Christen, A. Hoffmann, M. Straßburg, M. Dworzak, U. Haboeck, A. V. Rodina, *Phys. Status Solidi B* **2004**, *241*, 231–260.
[32] A. B. Djurišić, Y. H. Leung, *Small* **2006**, *2*, 944–961.
[33] H. Z. Xue, N. Pan, R. G. Zeng, M. Li, X. Sun, Z. J. Ding, X. P. Wang, J. G. Hou, *J. Phys. Chem. C* **2009**, *113*, 12715–12718.
[34] L. M. Li, C. C. Li, J. Zhang, Z. F. Du, B. S. Zou, H. C. Yu, Y. G. Wang, T. H. Wang, *Nanotechnology* **2007**, *18*, 225504.
[35] L. I. Berger, in: *CRC Handbook of Chemistry and Physics*, Internet Version 2007, 87th ed. (Ed.: D. R. Lide), Taylor and Francis, Boca Raton, FL (USA), **2007**, section 12, p. 83.
[36] W. I. Park, J. S. Kim, G.-C. Yi, M. H. Bae, H.-J. Lee, *Appl. Phys. Lett.* **2004**, *85*, 5052–5054.
[37] Z. Y. Fan, D. W. Wang, P.-C. Chang, W.-Y. Tseng, J. G. Lu, *Appl. Phys. Lett.* **2004**, *85*, 5923–5925.
[38] J. Goldberger, D. J. Sirbuly, M. Law, P. D. Yang, *J. Phys. Chem. B* **2005**, *109*, 9–14.
[39] Y. K. Park, A. Umar, E. W. Lee, D. M. Hong, Y.-B. Hahn, *J. Nanosci. Nanotechnol.* **2009**, *9*, 5745–5751.
[40] P.-C. Chang, C.-J. Chien, D. Stichtenoth, C. Ronning, J. G. Lu, *Appl. Phys. Lett.* **2007**, *90*, 113101.
[41] P. Nguyen, H. T. Ng, T. Yamada, M. K. Smith, J. Li, J. Han, M. Meyyappan, *Nano Lett.* **2004**, *4*, 651–657.
[42] T. Bryllert, L.-E. Wernersson, T. Löwgren, L. Samuelson, *Nanotechnology* **2006**, *17*, S227.
[43] A. Lugstein, M. Steinmair, C. Henkel, E. Bertagnolli, *Nano Lett.* **2009**, *9*, 1830–1834.

Received: April 27, 2010
Published Online: August 27, 2010

